

Voltage-controlled magnetic anisotropy enabled by resistive switching

Pavel Salev^{1,*}, Iana Volvach,² Dayne Sasaki³, Pavel Lapa,¹ Yayoi Takamura³, Vitaliy Lomakin,² and Ivan K. Schuller¹

¹*Department of Physics, University of California San Diego, San Diego, California 92093, USA*

²*Center for Memory and Recording Research, University of California San Diego, San Diego, California 92093, USA*

³*Department of Materials Science and Engineering, University of California Davis, Davis, California 95616, USA*



(Received 30 December 2021; revised 15 April 2022; accepted 12 January 2023; published 15 February 2023)

The discovery of new mechanisms of controlling magnetic properties by electric fields or currents furthers the fundamental understanding of magnetism and has important implications for practical use. Here, we present an approach of utilizing resistive switching to control magnetic anisotropy. We study a ferromagnetic oxide that exhibits an electrically triggered metal-to-insulator phase transition producing a volatile resistive switching. The switching occurs in a characteristic spatial pattern, the formation of an insulating barrier perpendicular to the current flow, which results in an unusual ferromagnetic/paramagnetic/ferromagnetic configuration. The formation of this voltage-driven paramagnetic insulating barrier is accompanied by the emergence of a strong uniaxial magnetic anisotropy that overpowers the intrinsic material anisotropy. Our results demonstrate that resistive switching is an effective tool for manipulating magnetic properties. Because resistive switching can be induced in a broad range of materials, our findings could enable a new class of voltage-controlled magnetism systems.

DOI: [10.1103/PhysRevB.107.054415](https://doi.org/10.1103/PhysRevB.107.054415)

I. INTRODUCTION

Achieving efficient voltage-controlled magnetism remains one of the central efforts in the scientific and engineering communities [1–3]. Electrical manipulation of magnetization or Néel vector direction, magnetic anisotropy, coercivity, saturation magnetization, transition temperature, exchange bias field, etc., is crucial for building spintronic devices for applications in next generation information technology [4,5]. Proposals for electrical manipulation of magnetic properties include utilizing intrinsic and engineered multiferroics [6–9] or magnetoelectric heterostructures [10–13], field-effect devices with solid [14–17] or electrolyte [18–20] gates, magnetoionic systems [21–23], and exchange bias heterostructures [24–26]. In this work, we present a concept of using resistive switching to enable voltage-controlled magnetic anisotropy (VCMA). Resistive switching allows changing a material's resistivity by applying voltage/current. This phenomenon attracted great attention because of the possible applications in conventional binary memories and synapselike memories for neuromorphic hardware [27,28]. Typically, resistive switching occurs in characteristic spatial patterns resulting in the conducting/insulating regions' coexistence. A common example of such a pattern is a conducting filament percolating through an insulating matrix [29,30]. Here we demonstrate that the resistive-switching-driven formation of conducting/insulating regions in a magnetic oxide, which creates the concomitant ferromagnetic (FM)/paramagnetic (PM) pattern, induces strong uniaxial magnetic anisotropy. This anisotropy closely follows the switching and can be reversibly turned on/off.

Our work shows that employing resistive switching is a viable strategy to achieve voltage-controlled magnetism, which potentially could be implemented in a variety of ferro-, ferri-, and antiferromagnetic materials.

II. EXPERIMENTAL RESULTS

We explored the resistive switching impact on magnetic properties in $\text{La}_{0.7}\text{Sr}_{0.3}\text{MnO}_3$ (LSMO) using planar $50 \times 100 \mu\text{m}^2$ two-terminal devices. Structural and electrical characterization of the sample is available in the Supplemental Material [31] (Figs. S1 and S2). LSMO has a phase transition at $T_c \approx 340$ K from a low-temperature FM metal to a high-temperature PM insulator. We showed recently that voltage application can trigger the coupled metal-to-insulator and FM-to-PM transitions producing volatile resistive switching, i.e., a switching that automatically resets upon removing voltage [32]. This switching is driven by Joule heating as the highly nonlinear resistance-temperature dependence of LSMO leads to thermal runaway at high applied voltages. On the microscopic level, the metal-to-insulator switching occurs by the formation of a PM insulating barrier perpendicular to the electric current. Figures 1(a) and 1(b) demonstrate the barrier formation. The I - V characteristics of the device [Fig. 1(a)] exhibits a negative differential resistance above 13 V, which is a signature of resistive switching. Spatially resolved magneto-optical Kerr effect (MOKE) measurements showed that during the switching, the uniform FM state [Fig. 1(b), blue line] transforms into a state that has a PM barrier in the device center [Fig. 1(b), red line]. Details of the measurement setup and data interpretation are available elsewhere [32]. Inside this barrier, the MOKE signal completely vanishes. Outside the barrier, the device remains FM and the MOKE signal is comparable to its value in equilibrium. Magnetic anisotropy

*Present address: Department of Physics and Astronomy, University of Denver, Denver, Colorado 80208, USA; pavel.salev@du.edu

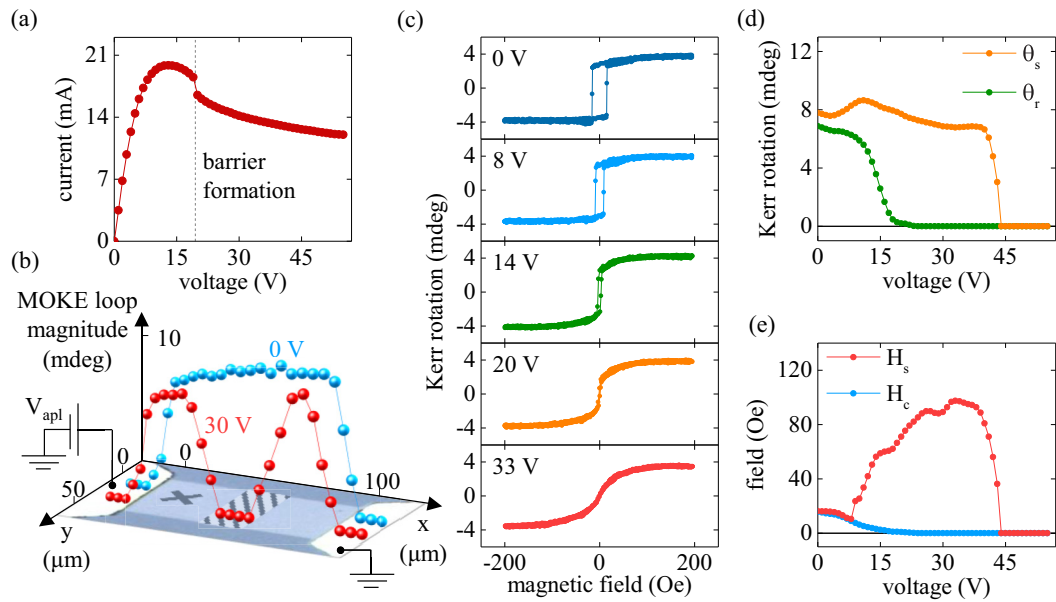


FIG. 1. (a) I - V curve of an LSMO device showing volatile resistive switching. (b) MOKE loop amplitudes recorded along the device length in equilibrium (blue line) and during the switching (red line). The curves are overlaid with the device optical image. At 30 V, zero MOKE signal indicates the PM insulating barrier formation at the device center. (c) MOKE loops recorded at a spot close to one of the electrodes [marked by a cross in (b)] at several applied voltages. As the voltage drives the device through resistive switching, the loops become oblique indicating the change of magnetic anisotropy. (d), (e) MOKE saturation θ_s and remanence θ_r , (d) and coercive H_c and saturation fields H_s (e) as functions of voltage. The values of θ_s , θ_r , H_c , and H_s were extracted from individual MOKE loops recorded at different applied voltages. All measurements were performed at 100 K.

change in the FM regions surrounding the PM barrier is the focus of this paper.

Resistive switching in LSMO produces a strong VCMA effect as evidenced by the pronounced change of the hysteresis loop shape. Figure 1(c) shows the MOKE loops' evolution under applied voltage. The loops were recorded using a 5- μm -size laser beam focused at a spot near one of the electrodes [marked by a cross in Fig. 1(b)]. The measurement spot was approximately 40 μm away from the PM insulating barrier formation position. Magnetic field was applied along the device length. While ramping up the voltage in the 0–8-V range, we observed square hysteresis loops. The only noticeable change at these voltages is the $\sim 40\%$ coercivity reduction. This reduction is likely due to the temperature increase caused by the uniform Joule heating that precedes the switching [32]. In the 8–20-V range, the nonlinearities and development of negative differential resistance in the I - V curve [Fig. 1(a)] indicate that the voltage and dissipated power distributions in the device becomes inhomogeneous [32,33] eventually culminating in the formation of a PM insulating barrier that further focuses the applied voltage and power. At the same time the hysteresis shape changes from square to oblique. After the barrier formation at 20 V where the I - V curve displays a small discontinuity, the coercivity and remanence vanish resulting in a nonhysteretic MOKE loop. Because resistive switching in the LSMO devices is volatile, removing the applied voltage resets the device and restores the initial square loop. The voltage-induced hysteresis shape changes differ qualitatively from the equilibrium temperature evolution (Fig. S3 in the Supplemental Material [31]), therefore our observations cannot be attributed to simple Joule heating increasing the

device temperature. The experimental results also cannot be explained by the Oersted field generation due to the current flowing in the device. As the device undergoes the metal-to-insulator switching, the current decreases with increasing voltage [Fig. 1(a)], while the suppression of hysteresis loop squareness becomes more pronounced [Fig. 1(c)], which is inconsistent with the effect of current-induced magnetic fields. The hysteresis loop change from the square to oblique shape indicates the development of a hard magnetic anisotropy along the device length during the switching. The overall impact of this voltage-induced anisotropy in the LSMO devices, i.e., the complete suppression of coercivity and remanence, can be qualitatively compared to the best examples of VCMA in magnetoelectric [11] and magnetoionic [21,22] devices.

The resistive-switching-driven VCMA occurs without a considerable suppression of the FM state. The Kerr rotation values corresponding to magnetic saturation at the maximum applied field, θ_s , has a weak voltage dependence [Fig. 1(d), orange line]. Only when the applied voltage becomes large enough to drive the material into the PM state does the MOKE signal plummet to zero and no sign of ferromagnetism can be observed. The remanence value at zero field in the MOKE loops, θ_r , on the other hand, rapidly decreases as the device undergoes resistive switching [Fig. 1(d), green line]. Because the remanence becomes zero without a noticeable change of the saturation, the observed VCMA cannot be attributed to the applied voltage driving the device on the verge of the PM transition where the uniform magnetization state might not be stable. Instead, the measurements show evidence that as the resistive switching progresses, an internal magnetic field develops along the device length. Figure 1(e) compares

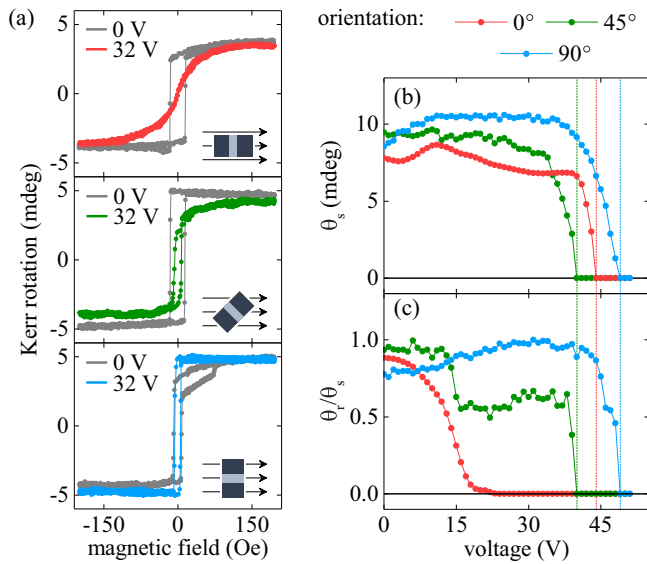


FIG. 2. (a) MOKE loops recorded at equilibrium (grey lines) and during resistive switching (color lines) using magnetic field at the three orientations with respect to the device length (schematically shown in the pictograms). (b), (c) MOKE saturation θ_s , (b) and remanence ratio θ_r/θ_s , (c) as functions of voltage for the three orientations. The values of θ_s and θ_r were extracted from individual MOKE loops recorded at different applied voltages. All measurements were performed at 100 K.

coercive H_c and saturation fields H_s (calculated as a field at which Kerr rotation value reaches 90% of the saturation θ_s). At low voltages, the saturation field closely tracks the coercive field. At the onset of resistive switching at 8 V, the saturation field begins to grow rapidly and eventually reaches the maximum of ~ 100 Oe, which is a factor of ~ 5 increase compared to its equilibrium value. Such a large saturation field increase suggests that the external magnetic field must overcome a strong opposing internal field. Because this internal field greatly exceeds the coercivity, the remnant uniform magnetization state becomes unstable producing the observed oblique, nonhysteretic MOKE loops.

MOKE measurements at different sample orientations provide an insight into the anisotropy change induced by resistive switching. Figure 2(a) compares the hysteresis loops acquired with the magnetic field oriented at 0° , 45° , and 90° with respect to the device length. Similar to data in Fig. 1, the loops were acquired at a spot close to one of the electrodes, i.e., away from the location where the PM insulating barrier initially forms during the switching. At zero voltage [grey loops in Fig. 2(a)], the loops along all three orientations have high squareness. Small shape variations between the three loops indicate the presence of an anisotropy that can be due to the intrinsic magnetocrystalline anisotropy of LSMO along the (110) crystallographic direction or extrinsic effects such as epitaxial strain and film morphology [34–36]. Importantly, the anisotropy at zero applied voltage is weak and the device can be easily magnetized in any in-plane direction. During resistive switching, the hysteresis shape depends strongly on the device orientation in the magnetic field [color loops in

Fig. 2(a)]. While the loops at 0° and 45° show a similar trend—squareness suppression under applied voltage—the loop at 90° displays squareness enhancement. Figures 2(b) and 2(c) summarize the dependence of the Kerr rotation value at magnetic saturation, θ_s , and remanence ratio, θ_r/θ_s , for the three orientations. θ_s displays a similar trend in all three orientations [Fig. 2(b)]: it remains nearly unchanged until a critical voltage at which the PM insulating barrier expands to the hysteresis measurement coordinate causing a rapid drop of the measured Kerr signal. Because the sample was manually reattached for every orientation, the location of the MOKE measurement spot differed slightly, resulting in slight critical voltage variations. A small measurement coordinate uncertainty does not impact the results' interpretation because the loops have a nearly identical shape everywhere inside the FM regions (Figs. S4 and S5 [31]). The orientation insensitivity of the θ_s voltage dependence can be explained by taking into account that the device temperature, which determines the saturation magnetization and θ_s , is controlled by Joule heating generated during resistive switching. The direction of applied magnetic field cannot strongly influence Joule heating. The remanence ratio vs voltage dependence, on the other hand, clearly shows the VCMA. Initially, the remanence ratio is close to 1 in all three orientations. When the voltage triggers resistive switching, the remanence ratio drops to zero at the 0° orientation, decreases to ~ 0.6 – 0.7 at 45° and becomes ~ 1 at 90° , suggesting a sinusoidal angular dependence. The orientation-dependent MOKE measurements thus indicate the development of a uniaxial anisotropy in the direction perpendicular to the device length during the metal-to-insulator switching.

The VCMA is most efficient at low temperatures. Figure 3(a) compares the hysteresis loops recorded in equilibrium ($V = 0$) and during resistive switching ($V > V_{sw}$) at three temperatures. Because the voltage V_{sw} that induces switching in LSMO is temperature dependent [32], the MOKE loops at different temperatures were measured under different applied voltages, $V > V_{sw}$, adjusted to maximize the VCMA effect, 48, 29, and 11 V for 50, 200, and 300 K, respectively. At 50 K, the applied voltage causes the complete remanence and coercivity suppression and strongly increases the saturation field leading to a highly oblique MOKE loop. At 200 K, a substantial decrease of the remanence and coercivity is induced during the switching, however, the saturation field remains close to its initial value at zero voltage. At 300 K, the applied voltage has no noticeable impact on the hysteresis loop shape. The VCMA correlates well with the temperature behavior of the resistive switching [Fig. 3(b)]. At low temperatures where the VCMA is strong, the I - V curves manifest a highly pronounced negative differential resistance, which is a characteristic property of resistive switching. As the temperatures increases, the negative differential resistance region first becomes shallow and then eventually disappears. This gradual disappearance of pronounced nonlinear features in the I - V characteristics coincides with the decreasing VCMA. The correlation between the electric and magnetic temperature behaviors provides strong evidence that resistive switching is the driving force behind the observed VCMA in LSMO.

To quantitatively characterize the VCMA temperature dependence, we plot the resistive switching impact on the

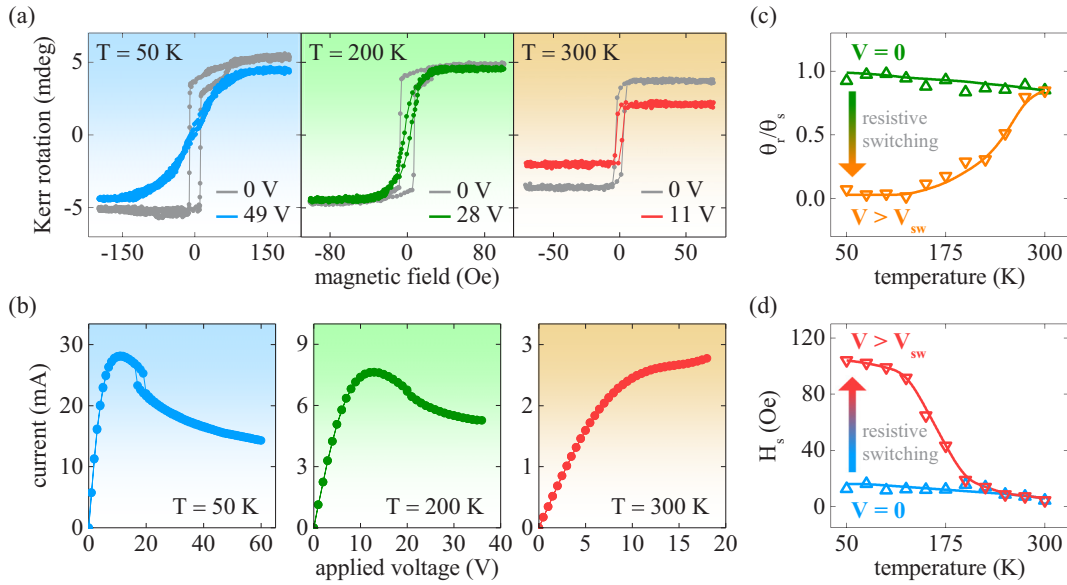


FIG. 3. (a) MOKE hysteresis loops recorded at equilibrium (grey lines) and during the resistive switching (color lines) at three different temperatures. The VCMA effect during the resistive switching is strong at 50 K, moderate at 200 K, weak or absent at 300 K. (b) I - V curves recorded at the same temperatures as the loops in (a). As temperature increases, the nonlinear behavior associated with resistive switching (especially the negative differential resistance) becomes less pronounced. (c) Temperature dependence of the remanence ratio θ_r/θ_s in equilibrium (green curve) and during resistive switching (orange curve). (d) Temperature dependence of the saturation field H_s in equilibrium (blue curve) and during resistive switching (red curve). In the panels, the points are experimental values and lines are guides to the eye. Individual points in the curves corresponding to resistive switching in (c) and (d) were obtained under applied voltages exceeding the minimum voltage V_{sw} that induces switching at each measurement temperature.

remanence ratio [Fig. 3(c)] and saturation field [Fig. 3(d)]. The individual points of the curves corresponding to resistive switching were obtained at progressively smaller applied voltages with increasing temperature to compensate for the temperature dependence of the switching in LSMO. At each temperature, the applied voltage was adjusted to maximize the VCMA effect. The remanence ratio at equilibrium is nearly independent of temperature and it is close to 1. By driving the device into the resistive switching state, the remanence ratio can be fully suppressed at temperatures below 150 K. At higher temperatures, only a partial remanence ratio suppression can be achieved during the switching. Near room temperature, applying voltage causes no noticeable remanence change, which indicates that the VCMA is either small or absent. The maximum saturation field under applied voltage vs temperature dependence shows two regimes [Fig. 3(d)]. Below 125 K, resistive switching leads to a factor of ~ 5 increase of the saturation field compared to its initial zero-voltage value. Above 200 K, the saturation field remains nearly unchanged during the switching, even though a moderate VCMA effect persists at least to 275 K as observed in the remanence vs temperature dependence [Fig. 3(c)]. This two-regime temperature behavior of the saturation field could be an indication that multiple mechanisms contribute to the VCMA. Using micromagnetic analysis, we investigated the effect of saturation magnetization variation due to temperature gradients produced by the resistive switching. Other possible mechanisms that can influence the VCMA include, for example, development of a crystal lattice strain due to thermal expansion and generation of spin currents due to temperature gradients.

III. MICROMAGNETIC SIMULATIONS

The micromagnetic simulations identified the important role of magnetostatic fields in the resistive-switching-induced VCMA. Simulation details are available in the Supplemental Material [31]. We considered a $500 \times 500 \times 10$ nm² FM slab subjected to a temperature gradient to emulate the PM insulating barrier formation effect during the switching [Fig. 4(a)]. This model represents a FM region of the LSMO device that experiences strong heating from the hot PM barrier and cooling from the cold electrode. Because the experimental temperature profile is unknown, we assumed a linear temperature gradient in our simulations in order to capture the basic physics. In the experiment, the MOKE signal inside the PM barrier vanishes indicating that the barrier temperature is above $T_c \sim 340$ K. The Kerr signal at magnetic saturation in the FM regions remains nearly unchanged suggesting that the FM region temperature is close to the base temperature of 100 K. We therefore used a $100 \rightarrow 340$ K gradient in the simulations. The temperature gradient produces a monotonic but nonlinear saturation magnetization decrease along the device length [Fig. 4(b)] due to the natural magnetization-temperature dependence. Because of this nonlinearity, rapid magnetization change occurs only in the hot region where temperature approaches T_c , making the model weakly dependent on a particular choice of the cold region temperature value. We used the experimental magnetization vs temperature dependence of an unpatterned LSMO film to represent the magnetization distribution in the model. We achieved excellent qualitative agreement between the measurements and simulations. Without the temperature gradient, the simulated

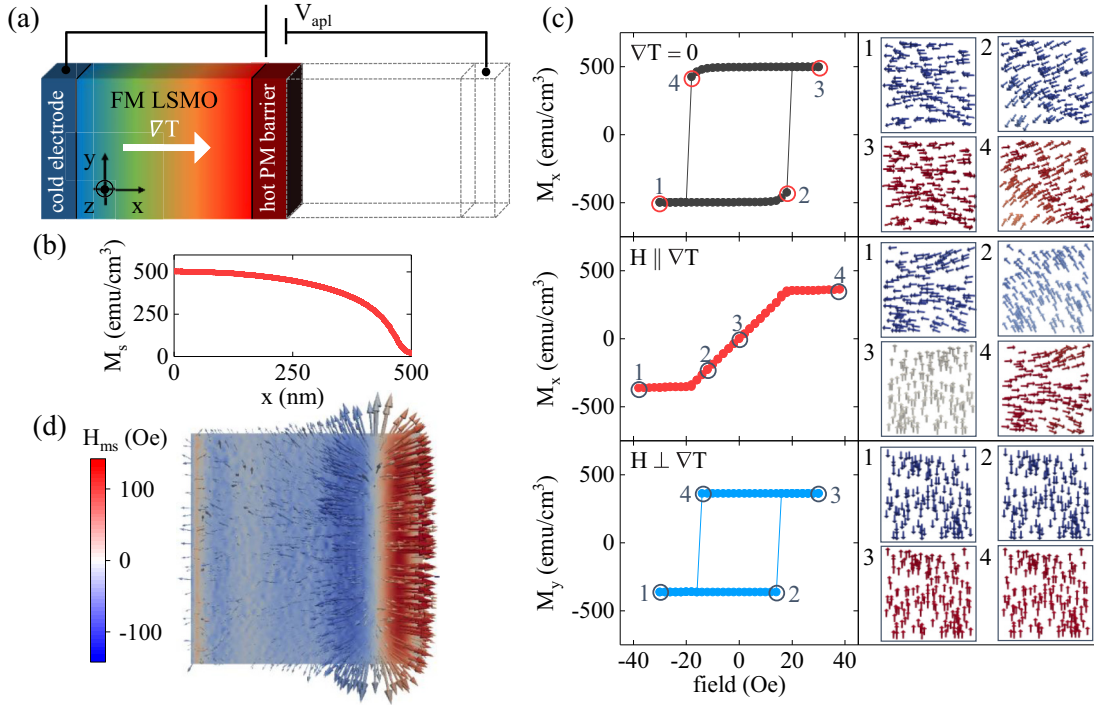


FIG. 4. (a) Model schematics: FM slab subjected to a linear temperature gradient. (b) Saturation magnetization spatial dependence used in the model to emulate the temperature gradient. (c) Left panels show simulated hysteresis loops without the temperature gradient (top) and with the magnetic field parallel (middle) and perpendicular (bottom) to the temperature gradient. Right panels show the calculated magnetization distribution at the numbered points in the hysteresis loops. (d) Magnetostatic field distribution when magnetization is saturated parallel to the temperature gradient (hot side on the right). Magnetization and magnetostatic field distribution plots in (c) and (d) show $500 \times 500 \text{ nm}^2$ area. Local hysteresis loops calculated in a $50 \times 50 \text{ nm}^2$ area in the center of $500 \times 500 \text{ nm}^2$ FM slab are shown in Fig. S6 [31].

loop has a square shape [Fig. 4(c), top] similar to the experimental loops recorded in equilibrium. With the temperature gradient, the simulated loop is oblique when the field is along the gradient [Fig. 4(c), middle] and the loop has an increased squareness when the field is perpendicular to the gradient [Fig. 4(c), bottom], reproducing the orientation-dependent measurements in Fig. 2.

The simulations reveal that the high-temperature FM region (i.e., the region next to the hot PM barrier) controls the magnetization reversal. In this region, the saturation magnetization rapidly changes leading to the emergence of an effective magnetostatic charge when there is a magnetization component along the temperature gradient, which, in turn, creates strong magnetostatic fields [Fig. 4(d)]. These magnetostatic fields can reach ~ 100 Oe in the region next to the effective charge, exceeding the intrinsic coercivity. The field direction is not uniform: the field is aligned with the magnetization in the closest proximity to the high-temperature PM barrier and the field and magnetization are antiparallel away from the barrier. The effective result of the magnetostatic fields is making the state with the magnetization along the temperature gradient energetically unfavorable. On the other hand, no magnetization components are created when there is no magnetization component along the temperature gradient, i.e., when the magnetization is saturated perpendicular to the temperature gradient (Fig. S7 [31]). The magnetization-orientation-dependent generation of magnetostatic charges acts as an anisotropy source. Because of this anisotropy, the hysteresis loop squareness is high in the direction perpendic-

ular to the temperature gradient (effective easy axis) and the squareness is low in the direction along the gradient (effective hard axis).

IV. DISCUSSION

The results of our micromagnetic simulations are reminiscent of the behavior in magnetization-graded materials [37–39]. In such materials, a spatial chemical composition variation produces a magnetization-graded profile strongly affecting the magnetic anisotropy. In the case of resistive switching, graded magnetization emerges due to the natural tendency of resistive switching to occur in spatially inhomogeneous patterns, allowing turning on/off and adjusting the magnetization-graded profile using voltage. As the voltage increases, the PM barrier expands and the magnetization gradient between the barrier and the electrode area is expected to become more extreme, which explains the VCMA effect increase with applied voltage observed in our LSMO devices [Fig. 1(c)]. Additionally, the magnetization gradient should be more pronounced in smaller size devices providing an opportunity to improve the efficiency of resistive switching driven VCMA.

Resistive switching control of magnetism potentially can be implemented in a variety of magnetic systems. The observed VCMA in LSMO is driven by the voltage-induced formation of a PM barrier inside the FM device, which is an immediate consequence of resistive switching, while the direct electric field effect on the magnetic order might

be negligible. Volatile switching due to the metal-insulator transition triggering (similar to this work) can be induced in other members of the manganite family that have FM and antiferromagnetic ordering [40,41], in antiferromagnetic V_2O_3 [42], and rare-earth nickelates [43]. Nonvolatile switching due to the electrically induced ionic migration has been demonstrated in FM (La,Sr)CoO₃ [44], antiferromagnetic SrFeO₃ [45], and ferrimagnetic Fe₃O₄ [46]. Resistive switching, volatile or nonvolatile, often occurs by the formation of conducting filaments [29,30] or insulating barriers [32,47], which would locally “inject” a different magnetic phase into an otherwise homogeneous material. Similar to this work, the filament/barrier formation can enable voltage-controlled magnetism in other resistive switching materials. Because of large device sizes used for the magneto-optical measurements and because of the electrothermal origin of the volatile switching in LSMO, the observed VCMA is accompanied by a substantial power consumption. Low-power high-speed operation at nanoscale has been demonstrated in a variety of

resistive switching systems [27], including volatile switching based on the metal-insulator transition triggering, potentially allowing the development of scalable energy-efficient VCMA devices. The interaction between resistive switching and magnetic order could be important for antiferromagnetic materials in which an efficient way to control the Néel vector is the key ingredient to enable a new class of spintronic devices [48].

ACKNOWLEDGMENTS

The magnetism research was supported by the U.S. Department of Energy (DOE), Office of Science, Basic Energy Sciences (BES), Materials Sciences and Engineering Division under Award No. DE-FG02-87ER45332. Material synthesis and numerical simulation were supported as a part of Quantum Materials for Energy Efficient Neuromorphic Computing (Q-MEEN-C), an Energy Frontier Research Center funded by the DOE, Office of Science, BES under Award No. DE-SC0019273.

-
- [1] C. Song, B. Cui, F. Li, X. Zhou, and F. Pan, Recent progress in voltage control of magnetism: Materials, mechanisms, and performance, *Prog. Mater. Sci.* **87**, 33 (2017).
- [2] A. Molinari, H. Hahn, and R. Kruk, Voltage-control of magnetism in all-solid-state and solid/liquid magnetoelectric composites, *Adv. Mater.* **31**, 1806662 (2019).
- [3] B. Rana and Y. Otani, Towards magnonic devices based on voltage-controlled magnetic anisotropy, *Commun. Phys.* **2**, 90 (2019).
- [4] E. Y. Vedmedenko, R. K. Kawakami, D. D. Sheka, P. Gambardella, A. Kirilyuk, A. Hirohata, C. Binek, O. Chubykalo-Fesenko, S. Sanvito, B. J. Kirby *et al.*, The 2020 magnetism roadmap, *J. Phys. D: Appl. Phys.* **53**, 453001 (2020).
- [5] A. Hirohata, K. Yamada, Y. Nakatani, I.-L. Prejbeanu, B. Diény, P. Pirro, and B. Hillebrands, Review on spintronics: Principles and device applications, *J. Magn. Magn. Mater.* **509**, 166711 (2020).
- [6] Y. Tokunaga, Y. Taguchi, T. Arima, and Y. Tokura, Electric-field-induced generation and reversal of ferromagnetic moment in ferrites, *Nat. Phys.* **8**, 838 (2012).
- [7] J. T. Heron, J. L. Bosse, Q. He, Y. Gao, M. Trassin, L. Ye, J. D. Clarkson, C. Wang, J. Liu, S. Salahuddin *et al.*, Deterministic switching of ferromagnetism at room temperature using an electric field, *Nature (London)* **516**, 370 (2014).
- [8] S.-J. Chang, M.-H. Chung, M.-Y. Kao, S.-F. Lee, Y.-H. Yu, C.-C. Kaun, T. Nakamura, N. Sasabe, S.-J. Chu, and Y.-C. Tseng, GdFe_{0.8}Ni_{0.2}O₃: A multiferroic material for low-power spintronic devices with high storage capacity, *ACS Appl. Mater. Interfaces* **11**, 31562 (2019).
- [9] A. Mahmood, W. Echtenkamp, M. Street, J.-L. Wang, S. Cao, T. Komesu, P. A. Dowben, P. Buragohain, H. Lu, A. Gruverman *et al.*, Voltage controlled Néel vector rotation in zero magnetic field, *Nat. Commun.* **12**, 1674 (2021).
- [10] R. O. Cherifi, V. Ivanovskaya, L. C. Phillips, A. Zobelli, I. C. Infante, E. Jacquet, V. Garcia, S. Fusil, P. R. Bridson, N. Guiblin *et al.*, Electric-field control of magnetic order above room temperature, *Nat. Mater.* **13**, 345 (2014).
- [11] J. Lou, M. Liu, D. Reed, Y. Ren, and N. X. Sun, Giant electric field tuning of magnetism in novel multiferroic FeGaB/lead zinc niobate-lead titanate (PZN-PT) heterostructures, *Adv. Mater.* **21**, 4711 (2009).
- [12] T. Nan, Y. Lee, S. Zhuang, Z. Hu, J. D. Clarkson, X. Wang, C. Ko, H. Choe, Z. Chen, D. Budil *et al.*, Electric-field control of spin dynamics during magnetic phase transitions, *Sci. Adv.* **6**, eabd2613 (2020).
- [13] R. V. Chopdekar, M. Buzzi, C. Jenkins, E. Arenholz, F. Nolting, and Y. Takamura, Giant reversible anisotropy changes at room temperature in a (La,Sr)MnO₃/Pb(Mg,Nb,Ti)O₃ magnetoelectric heterostructure, *Sci. Rep.* **6**, 27501 (2016).
- [14] H. Ohno, D. Chiba, F. Matsukura, T. Omiya, E. Abe, T. Dietl, Y. Ohno, and K. Ohtani, Electric-field control of ferromagnetism, *Nature (London)* **408**, 944 (2000).
- [15] S. Jiang, J. Shan, and K. F. Mak, Electric-field switching of two-dimensional van der Waals magnets, *Nat. Mater.* **17**, 406 (2018).
- [16] H. J. A. Molegraaf, J. Hoffman, C. A. F. Vaz, S. Gariglio, D. van der Marel, C. H. Ahn, and J.-M. Triscone, Magnetoelectric effects in complex oxides with competing ground states, *Adv. Mater.* **21**, 3470 (2009).
- [17] H. Lu, T. A. George, Y. Wang, I. Ketsman, J. D. Burton, C.-W. Bark, S. Ryu, D. J. Kim, J. Wang, C. Binek *et al.*, Electric modulation of magnetization at the BaTiO₃/La_{0.67}Sr_{0.33}MnO₃ Interfaces, *Appl. Phys. Lett.* **100**, 232904 (2012).
- [18] M. Weisheit, S. Fahler, A. Marty, Y. Souche, C. Poinignon, and D. Givord, Electric field-induced modification of magnetism in thin-film ferromagnets, *Science* **315**, 349 (2007).
- [19] A. Quintana, J. Zhang, E. Isarain-Chávez, E. Menéndez, R. Cuadrado, R. Robles, M. D. Baró, M. Guerrero, S. Pané, B. J. Nelson *et al.*, Voltage-induced coercivity reduction in nanoporous alloy films: A boost toward energy-efficient magnetic actuation, *Adv. Funct. Mater.* **27**, 1701904 (2017).
- [20] J. Walter, B. Voigt, E. Day-Roberts, K. Heltemes, R. M. Fernandes, T. Birol, and C. Leighton, Voltage-induced ferromagnetism in a diamagnet, *Sci. Adv.* **6**, eabb7721 (2020).
- [21] C. Bi, Y. Liu, T. Newhouse-Illige, M. Xu, M. Rosales, J. W. Freeland, O. Mryasov, S. Zhang, S. G. E. te Velthuis, and W. G.

- Wang, Reversible Control of Co Magnetism by Voltage-Induced Oxidation, *Phys. Rev. Lett.* **113**, 267202 (2014).
- [22] U. Bauer, L. Yao, A. J. Tan, P. Agrawal, S. Emori, H. L. Tuller, S. van Dijken, and G. S. D. Beach, Magneto-ionic control of interfacial magnetism, *Nat. Mater.* **14**, 174 (2015).
- [23] S. Ning, Q. Zhang, C. Occhialini, R. Comin, X. Zhong, and C. A. Ross, Voltage control of magnetism above room temperature in epitaxial Sr Co_{1-x}Fe_xO_{3-δ}, *ACS Nano* **14**, 8949 (2020).
- [24] S. M. Wu, S. A. Cybart, P. Yu, M. D. Rossell, J. X. Zhang, R. Ramesh, and R. C. Dynes, Reversible electric control of exchange bias in a multiferroic field-effect device, *Nat. Mater.* **9**, 756 (2010).
- [25] A. Chen, Y. Zhao, P. Li, X. Zhang, R. Peng, H. Huang, L. Zou, X. Zheng, S. Zhang, P. Miao *et al.*, Angular dependence of exchange bias and magnetization reversal controlled by electric-field-induced competing anisotropies, *Adv. Mater.* **28**, 363 (2016).
- [26] J.-L. Wang, W. Echtenkamp, A. Mahmood, and C. Binek, Voltage controlled magnetism in Cr₂O₃ based all-thin-film systems, *J. Magn. Magn. Mater.* **486**, 165262 (2019).
- [27] J. del Valle, J. G. Ramírez, M. J. Rozenberg, and I. K. Schuller, Challenges in materials and devices for resistive-switching-based neuromorphic computing, *J. Appl. Phys.* **124**, 211101 (2018).
- [28] Z. Wang, H. Wu, G. W. Burr, C. S. Hwang, K. L. Wang, Q. Xia, and J. J. Yang, Resistive switching materials for information processing, *Nat. Rev. Mater.* **5**, 173 (2020).
- [29] D.-H. Kwon, K. M. Kim, J. H. Jang, J. M. Jeon, M. H. Lee, G. H. Kim, X.-S. Li, G.-S. Park, B. Lee, S. Han *et al.*, Atomic structure of conducting nanofilaments in TiO₂ resistive switching memory, *Nat. Nanotechnol.* **5**, 148 (2010).
- [30] S. Kumar, M. D. Pickett, J. P. Strachan, G. Gibson, Y. Nishi, and R. S. Williams, Local temperature redistribution and structural transition during joule-heating-driven conductance switching in VO₂, *Adv. Mater.* **25**, 6128 (2013).
- [31] See Supplemental Material at <http://link.aps.org/supplemental/10.1103/PhysRevB.107.054415> for additional experimental and simulation data.
- [32] P. Salev, L. Fratino, D. Sasaki, R. Berkoun, J. del Valle, Y. Kalcheim, Y. Takamura, M. Rozenberg, and I. K. Schuller, Transverse barrier formation by electrical triggering of a metal-to-insulator transition, *Nat. Commun.* **12**, 5499 (2021).
- [33] B. K. Ridley, Specific negative resistance in solids, *Proc. Phys. Soc.* **82**, 954 (1963).
- [34] Y. Suzuki, H. Y. Hwang, S.-W. Cheong, and R. B. van Dover, The role of strain in magnetic anisotropy of manganite thin films, *Appl. Phys. Lett.* **71**, 140 (1997).
- [35] L. M. Berndt, V. Balbarin, and Y. Suzuki, Magnetic anisotropy and strain states of (001) and (110) colossal magnetoresistance thin films, *Appl. Phys. Lett.* **77**, 2903 (2000).
- [36] P. Perna, C. Rodrigo, E. Jiménez, F. J. Teran, N. Mikuszeit, L. Méchin, J. Camarero, and R. Miranda, Tailoring magnetic anisotropy in epitaxial half metallic La_{0.7}Sr_{0.3}MnO₃ thin films, *J. Appl. Phys.* **110**, 13919 (2011).
- [37] C. Sudakar, R. Naik, G. Lawes, J. V. Mantese, A. L. Micheli, G. Srinivasan, and S. P. Alpay, Internal magnetostatic potentials of magnetization-graded ferromagnetic materials, *Appl. Phys. Lett.* **90**, 62502 (2007).
- [38] D. Goll, A. Breitling, L. Gu, P. A. van Aken, and W. Sigle, Experimental realization of graded L1₀-FePt/Fe composite media with perpendicular magnetization, *J. Appl. Phys.* **104**, 83903 (2008).
- [39] L. Fallarino, B. J. Kirby, and E. E. Fullerton, Graded magnetic materials, *J. Phys. D: Appl. Phys.* **54**, 303002 (2021).
- [40] A. Asamitsu, Y. Tomioka, H. Kuwahara, and Y. Tokura, Current switching of resistive states in magnetoresistive manganites, *Nature (London)* **388**, 50 (1997).
- [41] M. Tokunaga, Y. Tokunaga, and T. Tamegai, Imaging of Percolative Conduction Paths and their Breakdown in Phase-Separated (La_{1-y}Pr_y)_{0.7}Ca_{0.3}MnO₃ with y = 0.7, *Phys. Rev. Lett.* **93**, 037203 (2004).
- [42] Y. Kalcheim, A. Camjayi, J. del Valle, P. Salev, M. Rozenberg, and I. K. Schuller, Non-thermal resistive switching in mott insulator nanowires, *Nat. Commun.* **11**, 2985 (2020).
- [43] N. Shukla, T. Joshi, S. Dasgupta, P. Borisov, D. Lederman, and S. Datta, Electrically induced insulator to metal transition in epitaxial SmNiO₃ thin films, *Appl. Phys. Lett.* **105**, 12108 (2014).
- [44] Y. J. Fu, F. J. Xia, Y. L. Jia, C. J. Jia, J. Y. Li, X. H. Dai, G. S. Fu, B. Y. Zhu, and B. T. Liu, Bipolar resistive switching behavior of La_{0.5}Sr_{0.5}CoO_{3-σ} films for nonvolatile memory applications, *Appl. Phys. Lett.* **104**, 223505 (2014).
- [45] V. R. Nallagatla, T. Heisig, C. Baeumer, V. Feyer, M. Jugovac, G. Zamborlini, C. M. Schneider, R. Waser, M. Kim, C. U. Jung, and R. Dittmann, Topotactic phase transition driving memristive behavior, *Adv. Mater.* **31**, 1903391 (2019).
- [46] A. Odagawa, Y. Katoh, Y. Kanzawa, Z. Wei, T. Mikawa, S. Muraoka, and T. Takagi, Electroforming and resistance-switching mechanism in a magnetite thin film, *Appl. Phys. Lett.* **91**, 133503 (2007).
- [47] S. Marinković, A. Fernández-Rodríguez, Collienne S, S. B. Alvarez, S. Melinte, B. Maiorov, G. Rius, X. Granados, N. Mestres, A. Palau, and A. V. Silhanek, Direct visualization of current-stimulated oxygen migration in YBa₂Cu₃O_{7-δ} thin films, *ACS Nano* **14**, 11765 (2020).
- [48] V. Baltz, A. Manchon, M. Tsoi, T. Moriyama, T. Ono, and Y. Tserkovnyak, Antiferromagnetic spintronics, *Rev. Mod. Phys.* **90**, 015005 (2018).